

Pentablock copolymer morphology dependent transport and its impact upon film swelling, proton conductivity, hydrogen fuel cell operation, vanadium flow battery function, and electroactive actuator performance

Fei Huang, Timothy D. Largier, Wenjian Zheng, Chris J. Cornelius*

Department of Chemical & Biomolecular Engineering, University of Nebraska-Lincoln, Lincoln, NE 68588, United States



ARTICLE INFO

Keywords:

Ionomer solution processing into films
Morphology
SAXS and TEM
Water swelling and ion transport
Fuel cell, flow battery, and actuator function

ABSTRACT

Ionomer composition and morphology impacts functional group distribution, water and ion-transport, and physical properties related to toughness, and degradation resistance. NEXAR MD9100 a pentablock copolymer (PBC) film morphology was dramatically altered when solution-cast into a film using tetrahydrofuran (THF) versus a cyclohexane: heptane (C:H) mixture. Film property and morphology changes were evaluated using Transmission Electron Microscopy (TEM), Small-Angle X-ray Scattering (SAXS), and electrochemical impedance spectroscopy. These changes were compared to Nafion 117 and Nafion 212. Average sulfonated inter-domain spacing through the film's thickness increased from 22.3 nm (C:H cast) to 30.5 nm (THF cast) that was estimated using SAXS. TEM revealed that PBC solution-cast films from C:H contained a random distribution of discrete sulfonated domains. An ordered PBC morphology consisting of lamella and hexagonally packed ion groups were created from a THF solution-cast film. These changes were attributed to favorable solvent-ionomer interactions during solvent evaporation and film densification. This ordered morphology led to increased conductivity (4.5 mS/cm versus 47.8 mS/cm), improved fuel cell power (19 mW/cm² versus 160 mW/cm²), enhanced ionomer actuation (3.0 cm versus 6.9 cm), and modest self-discharge improvements for a vanadium redox-flow battery. This study demonstrates that morphology impacts ionomer physical properties, transport, and device function.

1. Introduction

Ionomers are characterized by three principal attributes related to ion conductivity, hydrophilicity, and fixed charge carriers within an electrically neutral structure [1–3]. These materials contribute to very diverse fields such as electrodialysis, electrolysis, dialysis, biomedical, analytical chemistry, sensors, actuators, batteries, and fuel cells [4]. For example, a polymer-electrolyte fuel-cell (PEMFC) uses an ionomer to transport ions produced during the electrochemical conversion of H₂ and O₂ into electricity, water, and heat [5]. Nafion is considered a state-of-the-art membrane used within a PEMFC, ionomeric polymer-metal composite (IPMC), and vanadium redox flow battery (VRB) function. It is comprised of a tetrafluoroethylene backbone, and a perfluorovinylether side chain terminated with a sulfonic acid group. This functional group forms ion clusters that reorganize into a percolating network throughout the hydrophobic matrix. Its material limitations, high cost, and poor performance at low humidity and elevated temperatures (above 90 °C) have led to many alternative ionomer developmental efforts [6]. While challenges exist for Nafion and other ionomers, it has

been used to create IPMCs that are needed for biomimetic devices employed as artificial muscles and soft robots [7,8]. IPMC actuation occurs when an electric field generates an asymmetrical film stress when ion, water, or an ionic liquid is transported within it [9–11]. Furthermore, ionomers have been used to enable VRB function by separating V(II)/V(III) and V(IV)/V(V) redox couples in order to store chemical energy [12]. VRB function is dependent upon ionomers with high proton conductivity that are impermeable to vanadium ions; possess excellent chemical stability, and low electrical areal resistance between membrane and electrode [13].

Technological impacts have led to many ionomer research and development efforts seeking to improve their properties using morphology and composition [14–16]. Their properties are dependent upon the spatial arrangement of ionic and non-ionic domains [17]. For example, Zhao [18] and Lee [19] showed that longer hydrophilic domains within a sulfonated poly(ether ether ketone) (SPEEK) and poly(arylene ether sulfone)-b-polyimide triggered phase separation. This caused ion conductive domains to transition from random to a non-random morphology. The result was a remarkable increase in proton conductivity.

* Corresponding author.

E-mail address: ccornelius2@unl.edu (C.J. Cornelius).

Fan and Cornelius et al. studied the viscoelastic and gas transport properties of a series of multi-block sulfonated poly(arylene ether sulfone) (BPSH-BPS) as a function of block length (5k:5k, 10k:10k, and 15k:15k), relaxation time, and temperature [20]. The results revealed that BPSH-PBS 10k:10k ionomers formed a lamella morphology, which led to enhanced proton conductivity and gas permselectivity versus its random counterpart.

Ionomer film processing is an incredibly important to its properties and potentially attainable morphology. Solution-casting Nafion has been shown to have a large impact upon its film properties [16,21,22]. Ma et al. showed that Nafion films prepared from alcohol and water exhibited higher proton conductivity that was accompanied by undesirable increases in water uptake, and methanol permeability versus films created from dimethylacetamide (DMAc), dimethylformamide (DMF), and *N*-methylpyrrolidone (NMP). These varied properties were attributed to sulfonate domain aggregation differences caused by solvent quality [21]. Solvent-type and casting temperature of SPEEK [23] and Nafion [16] films created large differences in proton conductivity and chemical stability. Bebin and Galiano [24,25] demonstrated that solvent-cast sulfonated polysulfone (sPSU) films had twice the proton conductivity as compared to melt-extruded sPSU.

In this study, NEXAR MD9100 that is a penta-block copolymer (PBC) was solution-cast using tetrahydrofuran (THF), and a 1:1 volume ratio of cyclohexane: heptane (C:H). All PBC films had a fixed ion-exchange capacity of 1.0. Film morphology and properties were studied using TEM, SAXS, and electrochemical impedance spectroscopy. Solvent used to create a film produced dramatic morphology changes from random to non-random that improved transport and device function. Several PBC film properties were compared to commercially processed Nafion films.

2. Experimental

2.1. PBC solution-cast films and nafion

NEXAR MD9100 was provided by Kraton Polymers LLC, Houston, TX. This PBC ionomer's International Union of Pure and Applied Chemistry (IUPAC) name is poly[*t*-butylstyrene-*b*-ethylene-*alt*-propylene-*b*-sulfonatedstyrene-*b*-ethylene-*alt*-propylene-*b*-*t*-butylstyrene], which is abbreviated as tBS-EP-sPS-EP-tBS in this work. PBC is synthesized using an anionic polymerization technique, which is selectively sulfonated to a desired ion-exchange capacity (IEC) [26,27]. The *t*-butylstyrene, ethylene-*alt*-propylene, and *b*-sulfonated styrene ionomer blocks are abbreviated as tBS, EP, and sPS. This NEXAR MD9100 has an IEC of 1.0 (mmol SO₃H/g polymer). Nafion® perfluorinated membranes were purchased from Sigma Aldrich and used as received. Nafion-117 (N117) and Nafion-212 (N212) films had a nominal thickness of 7 mil (177.8 μm) and 2 mil (50.8 μm) with an IEC of 0.91. N117 was commercially produced using an optimized melt-extrusion process

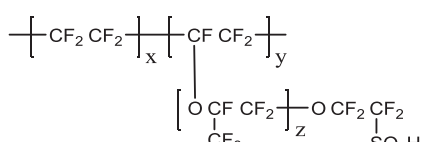
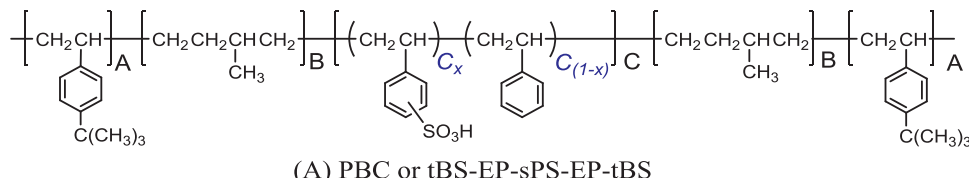


Table 1
PBC and Nafion film properties [26].

	IEC (mmol/g)	ρ (g/cm ³)	δ (J/cm ³) ^{1/2}	Processing method
N117	0.91	1.98	19.9	Melt-extrusion
N212	0.91	1.98	19.9	Solution-dispersion
PBC(C:H)	1.00	1.01	20.9	Solution-cast
PBC(THF)	1.00	1.01	20.9	Solution-cast

and N212 was created by a solution-dispersion technique. Their chemical structures are shown in Fig. 1.

A 2 wt% ionomer-solvent mixture was used to generate 90 μm PBC films used for this study. All tests were performed from the same solution-cast film to ensure material reproducibility. The solvents used to dissolve PBC were THF and C:H. This ionomer mixture was solution-cast within a Teflon mold (10 cm diameter) that was covered to control solvent evaporation rate over a four-day period at room temperature. Residual solvent and water was removed from a solid film using a vacuum oven at 35 °C for 24 h. PBC and Nafion film IEC, density (ρ), solubility parameter (δ), and film processing method are summarized in Table 1.

2.2. Morphology characterization

Small angle X-ray scattering (SAXS) and Transmission electron microscopy (TEM) were used to characterize PBC(C:H), PBC(THF), and Nafion-212 film morphology. SAXS measurements were gathered using a Rigaku Smartlab Diffractometer operating at 40 kV and 44 mA to produce a 1.542 Å wavelength (λ). The sample-to-detector distance was 30 cm, and the scattering vector (*q*) varied between 0.042 and 1.42 nm⁻¹. The value *q* is related to its scattering angle (θ), and x-ray wavelength (λ) using $q \equiv 4\pi/\lambda \sin[\theta/2]$. Average sulfonated inter-domain spacing (*d*) within a film was estimated based upon its maximum primary scattering peak (*q*_{max}) using the relationship $d = 2\pi/q_{max}$. TEM images were evaluated at 15,000x using a Hitachi H7500 operating at 80 kV using BaCl₂ stained PBC film slices. Films were stained using a 1 M BaCl₂ solution for 24 h, which preferentially interacted with sulfonated domains. Stained films were dried and then embedded within epoxy that was sectioned into 70 nm sections using a Leica UC7 ultra-microtome at room temperature. Sample

2.3. Conductivity measurements

All ionomer film proton conductivities were evaluated at 25 °C using a Metrohm Autolab PGSTAT302N potentiostat/galvanostat. In-plane measurements were conducted by clamping a rectangular membrane strip between two Pt electrodes in DI water. Through-plane measurements were done using two parallel stainless steel disks coated with Pt to clamp films that had a diameter of 0.526 cm. Nyquist

Fig. 1. A) PBC (NEXAR MD9100) with an IEC of 1.0; and B) Nafion structures for N117 and N212 with an IEC of 0.91.

impedance plots were collected from 0.1 Hz to 1.0 MHz. Temperature was controlled using an isothermal water bath (Thermo Scientific Inc.). This measurement was performed three times with less than 1% variation. Film sample conductivity variation was determined using three test samples from the larger test film. The sample conductivity variation was found to be less than 1%. Overall measurement error for data reported is less than 1%.

2.4. Water uptake and dimensional changes

PBC(C:H), PBC(THF), N117, and N212 film's initial mass (m_d) were evaluated after drying in a vacuum oven for 24 h. These dried films were equilibrated in DI water for three days prior to testing. A film's water swollen mass (m_w) was determined by quickly wiping excess water off its surface before a measurement. Water uptake (WU) was determined using Eq. (1). The WU sample to sample and repeated measurement variation was less than 2%.

$$\text{WU} = \left[\frac{m_w - m_d}{m_d} \right] \times 100 \quad (1)$$

A water swollen film's dimensional changes due to swelling in x , y , and z direction is defined using Eq. (2). The value Δl is the film's swollen/wet length (l_w) versus its "dry" original length (l_d). The ratio $\Delta l/l_d$ is the percent change in film length due to swelling. The film's thickness (z-direction) was measured with a digital micrometer with a 0.001 mm resolution and accuracy. The value $\Delta l/l_d$ variation was less than 2% in the z-direction, and much less in x and y .

$$\Delta l/l_d = \left[\frac{l_w - l_d}{l_d} \right] \times 100 \quad (2)$$

2.5. Hydrogen fuel cell performance

A membrane electrode assembly (MEA) was fabricated by spray coating a 20 wt% Pt/carbon slurry suspended within a 5 wt% Nafion solution onto PBC(C:H), PBC(THF), and N212. The final catalyst-coated membrane (CCM) anode and cathode electrode layers were designed to contain 0.5 mg/cm² Pt and 30 wt% Nafion. The anode and cathode electroactive area was 5 cm². The final cell was assembled using an optimized gas diffusion layer (GDL). Prior to testing, the cell was humidified for three hours and broken in over a 12-h period. Polarization data were collected by scanning the assembled fuel cell from open circuit voltage (OCV) to 0.1 V. The cell was operated at 80 °C and 100% RH using a H₂:O₂ stoichiometric ratio of 2:3, flow-rate of 300 SCCM (standard cubic centimeters per minute), and a back-pressure of 15 psig. Scans were repeated at least five times to ensure reproducibility prior to polarization data collection. Cyclic voltammetry (CV), and hydrogen crossover (CO) measurements were conducted to ensure MEA quality.

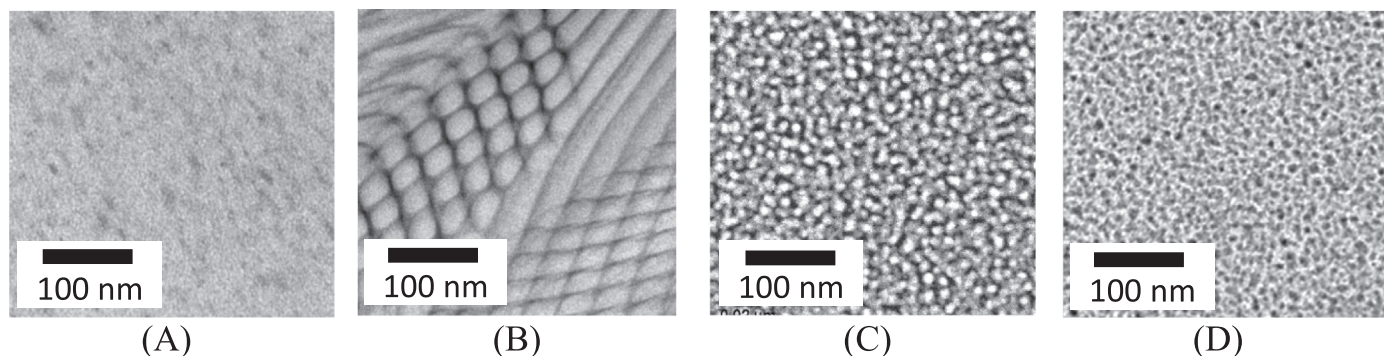


Fig. 2. Ionomer film TEM cross-sections of A) PBC(C:H), B) PBC(THF), C) N117, and D) N212.

2.6. Vanadium redox flow battery

PBC(C:H), PBC(THF), and N117 VRB performance was determined by creating individual 1 M VO₂⁺ and 1 M V²⁺ solutions dissolved in 2.5 M H₂SO₄ as the starting electrolyte. The test cell had copper current collectors coated with Au, and a graphite serpentine flow field with an effective area of 5 cm². Membranes were compressed 22% using a SIGRACELL® carbon felt (GFD4.5) and Teflon® gaskets. The positive and negative electrolyte tank volumes were 40 mL, and the solutions were circulated at 20 mL/minute. The electrolyte tanks were equipped with a N₂ purge due to V²⁺ reactivity with air. A constant 30 mA/cm² current was used to charge the cell to 1.7 V. A charge-discharge test was performed using terminal voltages between 1.7 V and 0.8 V at a current density of 10 mA/cm². An open circuit voltage (OCV) test was performed upon VRB cells that were charged to approximately 50% of their state-of-charge (SOC). The coulombic efficiency (η_{CE}), voltage efficiency (η_{VE}) and energy efficiency (η_{EE}) was calculated by evaluating a cell's discharge time (t_d), charging time (t_c), average discharging voltage (V_d), and average charging voltage (V_c). These relationships are given by Eqs. (3)–(5).

$$\eta_{CE} = \frac{t_d}{t_c} \cdot 100\% \quad (3)$$

$$\eta_{VE} = \frac{V_d}{V_c} \cdot 100\% \quad (4)$$

$$\eta_{EE} = \eta_{CE} \cdot \eta_{VE} \quad (5)$$

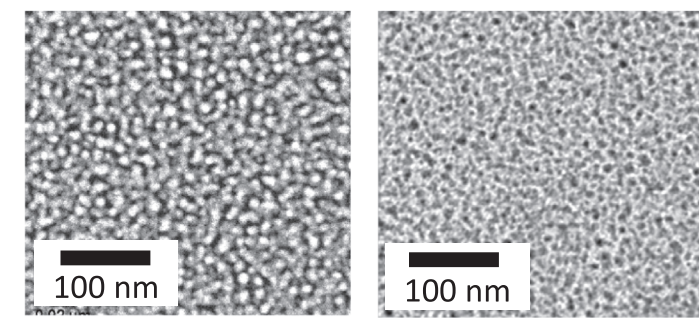
2.7. IPMC fabrication and actuation

PBC(C:H) and PBC(THF) film's surface was coated with a Pt⁺ salt by soaking it in 0.01 M Pt(NH₃)₄Cl₂ for 24 h. The Pt⁺ layer was reduced to Pt using a 5 wt% NaBH₄ solution. This electroless process was repeated twice to ensure a uniform metallic coating. The final processing step involved soaking a Pt coated PBC film in 2 M HCl, rinsing it in DI water, and soaking it in 1 M LiOH in order to create PBC(C:H)-Li⁺/Pt and PBC(THF)-Li⁺/Pt films. The IPMC actuator was designed to have a free bending length of 13.5 mm and 2 mm width. IPMC films were clamped between two Cu electrodes, and 3 V DC step voltages were used to induce bending. A CCD camera collected real-time tip bending displacements.

3. Results and discussion

3.1. Ionomer morphology, scattering properties, and predicted solution behavior

Ionomer film processing is critical to its morphology and physical properties. PBC(C:H), PBC(THF), N117, and N212 film morphology changes were evaluated using TEM and SAXS. TEM cross-sections of



PBC and Nafion films are shown in Fig. 2. Unsulfonated domains appear as lighter areas and sulfonated domains are darker due to preferential BaCl₂ staining. The PBC(C:H), N117, and N212 films have small and irregular shaped ion-domains that were randomly distributed throughout their matrix. Sulfonated domains within N117 and N212 were randomly distributed throughout its matrix shown in Fig. 2C and D that is consistent with other experimental efforts [2,15,16,28,29]. However, PBC(C:H) sulfonated domains appear farther apart and not as sharply defined as observed with Nafion (Fig. 2A). The PBC(THF) film had large-scale phase-separation between sulfonated and unsulfonated domains (Fig. 2B). A complex lamella-like morphology coexisting within hexagonally packed cylinders appeared to be more continuous within a film, and the sulfonated domains were more widely spaced with sharper contrast between ionic and non-ionic domains. These morphology differences are assumed to be associated with improved PBC solvation properties enabling greater polymer chain reorganization during solvent-casting.

PBC(THF) film morphology observed using TEM revealed that sulfonated domains were anisotropically distributed within a film. However, PBC(C:H), N117, and N212 random structure did not provide an obvious result corresponding to isotropic or anisotropic behavior. Consequently, SAXS was used to study these films in-plane (parallel to film) and through-plane (perpendicular to film) shown in Fig. 3. PBC(C:H) had a very broad scattering peak with maximums at $q = 0.204 \text{ nm}^{-1}$ (in-plane) and $q = 0.282 \text{ nm}^{-1}$ (through-plane), and no significant features observed at higher q . Directionally-dependent average inter-domain spacing was observed at $d = 30.8 \text{ nm}$ (in-plane) and $d = 22.3 \text{ nm}$ (through-plane), which indicates an anisotropic film. The film's diffuse scattering implies a disordered arrangement of sulfonated domains. This result is consistent with TEM (Fig. 2A) that revealed a random distribution of sulfonated domains that appear poorly connected. PBC(THF) films produced scattering peaks that were sharper and possessed additional features at higher q . The primary q occurred at a lower value corresponding to larger features, and the film had multiples (n) of q , which suggests a lamellar-like morphology [28]. The TEM effort revealed a film morphology consisting of lamella coexisting within a hexagonally packed structure (Fig. 2B). This organized

morphology produced sharper scattering peaks at $q = 0.146 \text{ nm}^{-1}$ (in-plane) and $q = 0.206 \text{ nm}^{-1}$ (through-plane) with additional peaks occurring at nq . The average inter-domain spacing was at $d = 43.0 \text{ nm}$ (in-plane) and $d = 30.5 \text{ nm}$ (through-plane). A common feature of both films was that the distance between sulfonated domains in-plane and through-plane was approximately 28% for both films. However, the d spacing between these domains was approximately 40% greater in-plane than through-plane for PBC(THF) versus PBC(C:H). These results reveal an orientation-dependent morphology that is caused by the solution-casting process that is affected by solvent type. N117 and N212 had a random morphology that produced nearly identical scattering in all directions. N117's in-plane and through-plane scattering peaks were 1.795 nm^{-1} and 1.806 nm^{-1} , which corresponds to an average sulfonated inter-domain spacings of $d = 3.50 \text{ nm}$ (in-plane) and $d = 3.48 \text{ nm}$ (through-plane). N112 had similar results with an average in-plane q and d values of 1.764 nm^{-1} and 3.56 nm , and through-plane values of 1.775 nm^{-1} and 3.54 nm . The ion domain spatial variation between in-plane and through-plane is approximately 0.6% for N117 and N112. This result suggests that ion-domains are isotropically distributed within a random morphology.

PBC(C:H) and PBC(THF) morphology differences at a fixed IEC are clearly associated with the type of solvent used to solution-cast a film. Flory-Huggins Solution Theory can be used to estimate solution thermodynamics. The theory takes into account molecule size to describe the entropy (ΔS_m) and enthalpy (ΔH_m) of mixing [34,42]. It assumes Regular Solution behavior, which implies little interaction between solvent and polymer molecules and flexible polymer chains. This also infers that solvent and polymer have similar δ values. The excess Gibbs Free Energy (ΔG_m) for mixing a polymer and solvent is described by $\Delta G_m = \Delta H_m - T\Delta S_m$. The value ΔH_m of a mixture is described using a solvent (ϕ_1) and polymer volume fraction (ϕ_2), chi parameter (χ_{12}), ideal gas constant (R), absolute temperature (T), and solvent molar volume (V_s) such that $\Delta H_m = \phi_1\phi_2\chi_{12}RT = \phi_1\phi_2Vs(\delta_1 - \delta_2)^2$. The χ_{12} value describes the interaction energy between polymer-solvent based upon the δ of ionomer and solvent. The entropy is represented by the number of solvent and polymer segments occupying a lattice space (r_1 and r_2) giving rise to the expression $\Delta S_m = R(\phi_1/r_1\ln\phi_1 + \phi_2/r_2\ln\phi_2)$. Utilizing

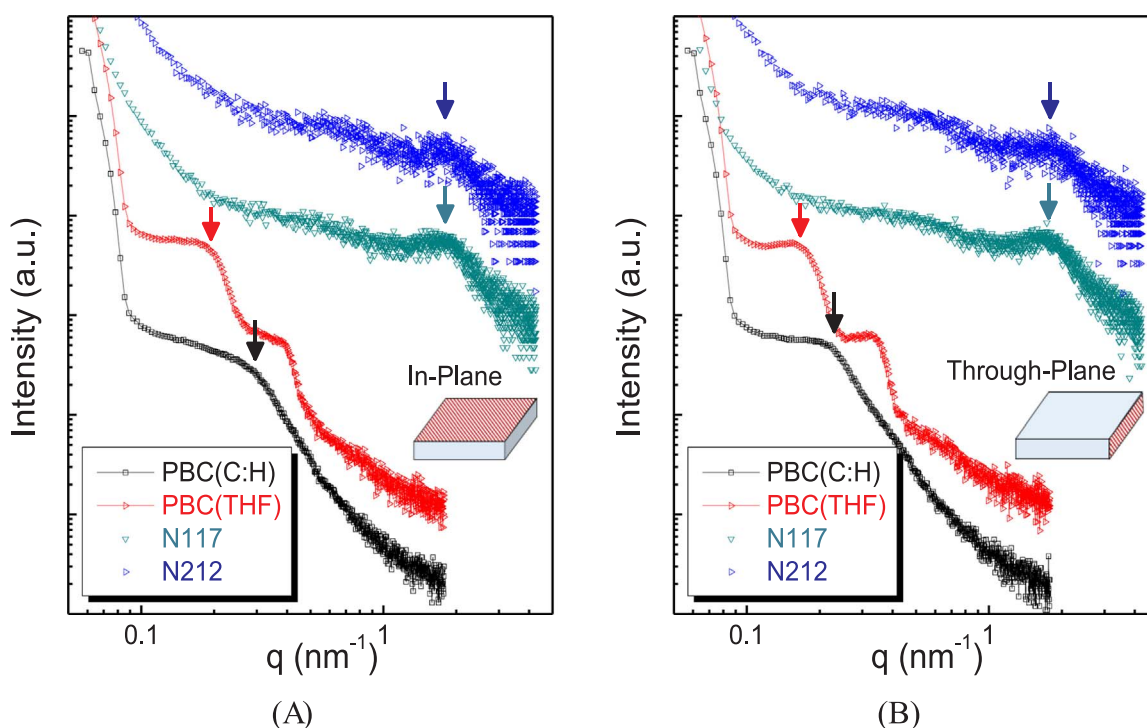


Fig. 3. PBC(C:H), PBC(THF), N117, and N212 directionally-dependent SAXS profiles for (A) in-plane and (B) through-plane.

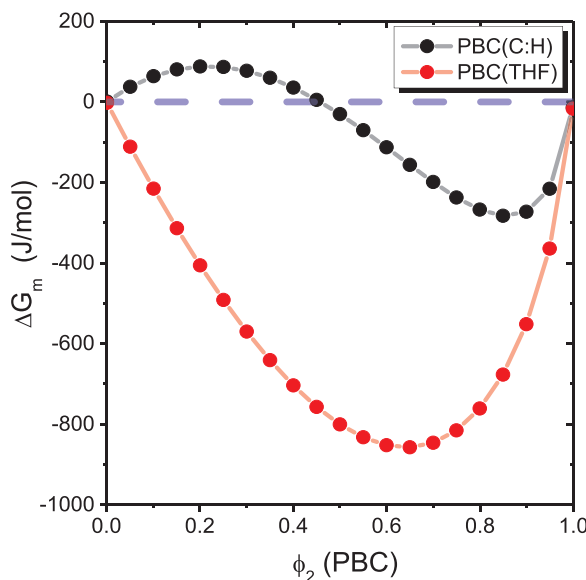


Fig. 4. Predicted ΔG_m thermodynamic behavior of PBC solutions containing C:H and THF as a function of concentration.

the equation $\chi_{12} = V_s/(RT)(\delta_1 - \delta_2)^2$ the predicted χ values for PBC dissolved into THF and C:H at 25 °C are 0.095 and 1.337. A small χ becomes very important as the solvent evaporates during film formation. During this process, strong interactions lead to ionomer chain aggregation and phase separation. This occurs in order to minimize ΔG_m for the mixture as it transitions from a dilute solution into a solid film during evaporation (Fig. 4). The change in ΔG_m during this process was ideally modeled and shown in Fig. 4. C:H is revealed as a favorable solvent for PBC1.0 at ϕ_1 less than 0.45 with a ΔG_m minimum (ΔG_m) of -283 J/mol at $\phi_2 = 0.85$. A PBC solution using THF had a ΔG_m of -858 J/mol at $\phi_2 = 0.65$, and ΔG_m is negative at all compositions, which predicts a favorable ionomer-solvent system. These thermodynamic predictions imply that THF may be a better solvent for PBC because it solvates chains better than C:H. This becomes pronounced during solvent removal during film densification.

Choi and Winey et al. [27] demonstrated that a PBC solution with an IEC = 1.0 using C:H contained dispersed micelles of sulfonated domains. These micelles have sPS as its core and the exterior chains primarily interacted with the solvent. This confirmation is adopted in order to lower its free energy to produce a more thermodynamically stable solution. The sulfonate group within PBC affects its hydrogen bonding and solvation characteristics. These solvent-ionomer dynamics will contribute to the formation of phase-separated structures during solution to film densification. These interaction forces would facilitate tBS, EP, and sPS solvation that would minimize micelle formation, promote chain extension, increase chain entanglements, and lower ΔG_m . This would be linked to ionomer morphology, ion-domain connectivity, and properties.

3.2. Ionomer water uptake

The WU properties N117, N212, and PBC(C:H) were found to be quite similar at 22.1 wt%, 23.1 wt%, and 24.6 wt% (Fig. 5). However, PBC(THF) non-random film morphology had a WU of 46 wt%, which is a doubling in this property as compared to PBC(C:H). This change is attributed a greater concentration of interconnected sulfonated domains. In order to probe this observation, group contribution method (GCM) and Hildebrand's Theory were used to estimate δ for PBC and Nafion [26,30]. PBC's predicted δ value was $20.9 \text{ (J/cm}^3)^{1/2}$ based upon tBS, EP, and sPS blocks at an IEC of 1.0. This value is consistent with numerous literature efforts [31–35]. Unfortunately, GCM does not account for spatial arrangement of groups, which is expected to

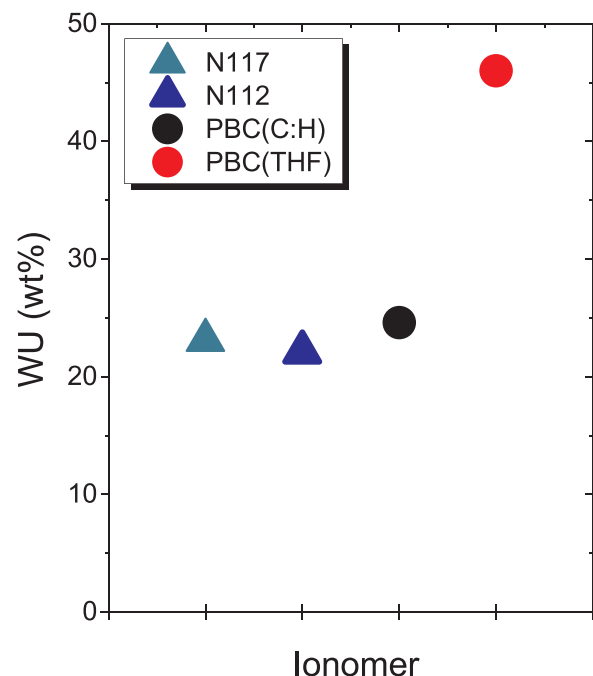


Fig. 5. Ionomer water uptake at 25 °C for N117, N212, PBC(C:H), and PBC(THF).

contribute to bulk properties. The estimated δ value for N117 and N212 was $19.9 \text{ (J/cm}^3)^{1/2}$ (Table 1). The predicted δ only varied by 5% for Nafion and PBC even though their experimental solubility characteristics are very different from one another. These results do not reveal the observed WU differences observed for these ionomers and in particular PBC(C:H) and PBC(THF).

The active ionomer chain concentration (n) involved with water swelling is influenced by ion group concentration (IEC), ρ , and ϕ_2 using the relationship $n_w = IEC \cdot \rho \cdot \phi_2 \text{ (mol/cm}^3)$. The estimated n_w value was rather constant for N117 ($1.24e-3 \text{ mol/cm}^3$) and N212 ($1.25e-3 \text{ mol/cm}^3$), but was 45% lower for PBC(C:H) ($6.89e-4 \text{ mol/cm}^3$) that is attributed to its lower IEC. PBC(THF) film's morphology transitioned from random to ordered that led to a WU increase from 24.6 wt% to 46 wt%, and n_w increasing 17% to $8.08e-4 \text{ mol/cm}^3$. The Flory-Rehner relationship was used to describe PBC(C:H), PBC(THF), N117, and N212 equilibrium swelling in water using n_w , ϕ_2 , and χ_{12} . The theory considers forces arising from ΔH_{mix} and ΔS_{mix} that impacts ionomer chain confirmation and elastic forces that can be ideally modeled using Eq. (6) [31–35].

$$-[ln(1-\phi_2) + \phi_2 + \chi_{12}\phi_2^2 = V_1 n \left[\phi_2^{1/3} - \frac{\phi_2}{2} \right]] \quad (6)$$

An ionomer's equilibrium swelling in a liquid or water can be used to estimate the χ_{12} assuming that n and ϕ_2 are known for it. Film morphology is expected to impact its swelling properties. Polymer solution to film formation during solvent evaporation was shown to lead to very different morphologies and water swelling between PBC(C:H) and PBC(THF). The lower swelling PBC(C:H) had a predicted χ_{12} of 1.233 that decreased to 0.957 for PBC(THF). These different values are attributed to the spatial arrangement of functional groups as noted with morphology. N117 and N212 had a χ_{12} value that is nominally 0.94. These results reveal that changes in morphology and composition impact swelling.

3.3. PBC directionally dependent water swelling

PBC and Nafion directionally dependent water swelling was evaluated in terms of axial film changes in x , y , and z . Film length changes

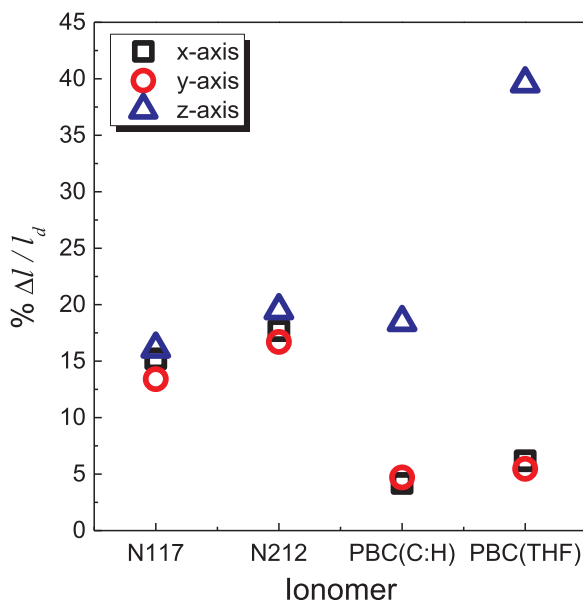


Fig. 6. N117, N212, PBC(C:H), and PBC(THF) film dimensional changes in *x*-axis, *y*-axis, and *z*-axis due to swelling in water at 25 °C.

were normalized and expressed as $\% \Delta l / l_d$ that is shown in [Fig. 6](#). PBC films produced using solution-casting had insignificant solvent transport in its *x*-axis and *y*-axis during evaporation. Consequently, film densification was dominated in the *z*-axis, or surface open to the atmosphere. This processing method created anisotropic films that swelled little in their *x*-axis and *y*-axis (parallel to casting surface). SAXS confirmed this film structure by a 40% increase in average *d* spacing between sulfonated domains in-plane versus through-plane. Film swelling in the *x*-axis and *y*-axis increased 4.17% and 4.88% for PBC(C:H), and 6.18% (*x*-axis) and 5.23% (*y*-axis) for PBC(THF). These similar spatial length changes are due to processing method. Film swelling in the *z*-axis increased 18.5% for PBC(C:H), and 39.6% for PBC(THF). The *z*-axis swelling difference between PBC(C:H) and PBC(THF) films is 114%. This significant change is attributed to morphology transitioning from random to a more ordered material, which led to a remarkable increase in water uptake (24.6 wt% versus 46 wt%). As previously noted, this is due to enhanced sulfonate group clustering that created a mixed morphology of lamella and hexagonally packed domains. Unlike solution-cast PBC films, N117 and N212 have been optimized in terms of processing based upon melt-extrusion and solution-dispersion techniques. The impacts of this processing effort are nominally isotropic films. A commercial N117 film swelled 15.2%, 13.4%, and 16.1% in its *x*, *y*, and *z* axes. A similar result was noted for Nafion212, which swelled 17.7%, 16.7%, and 19.5% in its *x*, *y*, and *z* axes. The N212 film changes are 10% larger than N117 that is attributed to film creation technique differences associated with extruding versus solution-dispersion. Overall, these results reveal that film processing and morphology have a large impact upon its dimensional changes.

3.4. Directionally-dependent film proton conductivity

PBC films were shown to transition from a random morphology to a non-random lamellar/hexagonal structure with anisotropic scattering and water swelling. The PBC(C:H) and PBC(THF) directionally-dependent proton conductivity were evaluated along their in-plane and through-plane directions ([Fig. 7](#)). The in-plane film conductivity of PBC(C:H) was 4.5 mS/cm, which increased to 47.8 mS/cm for a PBC(THF). This 962% conductivity improvement is attributed to a transformation from a random distribution of sulfonated domains to an ordered morphology. This is attributed to greater sulfonated domain

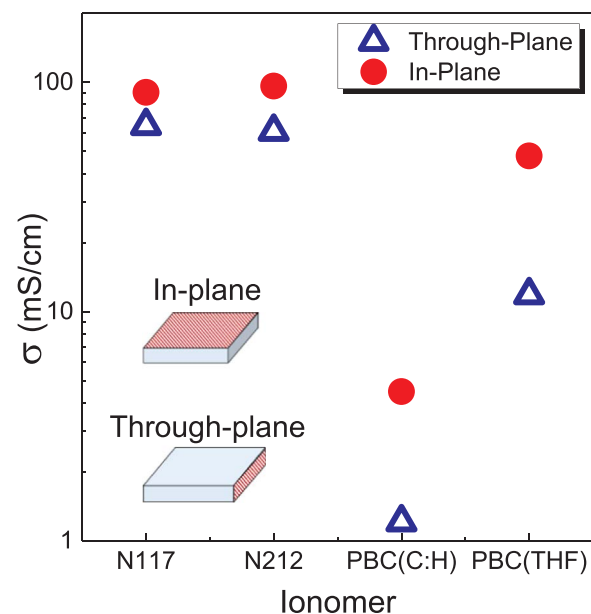


Fig. 7. N117, N212, PBC(C:H), and PBC(THF) proton conductivity measured at 25 °C in DI water.

connectivity within a PBC(THF) film that occurs with this lamella-like/hexagonally packed morphology. The film's through-plane conductivity was 1.2 mS/cm for PBC(C:H) and 11.8 mS/cm for PBC(THF). Its anisotropic conductivity differences are consistent with its directionally-dependent water swelling, and scattering properties observed using SAXS. However, the conductivity of PBC(THF) is an order of magnitude larger than PBC(C:H) in this direction. The in-plane and through-plane conductivity of N117 was 90.4 mS/cm and 64.7 mS/cm; and N112 was 96.3 mS/cm and 61.1 mS/cm at these conditions. This technique clearly reveals that both Nafion films have anisotropic conductivity that is not marginally noted using water swelling and SAXS. While N117 and N112 film production methods have been optimized using melt-extrusion and solution-dispersion, they still have anisotropic properties. These results demonstrate that conductivity is highly dependent upon casting solvent, solution-casting method, processing conditions, and morphology.

3.5. PBC and N212 hydrogen fuel cell performance

PBC morphology and the distribution of sulfonated domains within a film were shown to affect swelling and ion transport. These morphological changes improved ion-domain connectivity. This morphology enhancement is believed to impact electro-chemical function within a proton-exchange membrane fuel-cell (PEMFC). PBC(C:H) and PBC(THF) were compared to the PEMFC performance using N212 because of its properties were optimized for this application. A PBC(THF) based MEA produced a peak power of 160 mW/cm² at 360 mA/cm² at 80 °C as shown in [Fig. 8A](#). The PBC(C:H) based MEA only achieved a maximum power density of 19 mW/cm² at 45 mA/cm². These PEMFC output power increases were associated with an order-of-magnitude CCM interfacial resistance decrease from 6.4 Ω·cm² for PBC(C:H) to 0.65 Ω·cm² using PBC(THF). Lower membrane-electrode resistance is desirable because larger values are associated with increasing power losses due to resistive heating versus ion transport. The dramatic PEMFC change is attributed to an ordered morphology that led to improved proton transport properties (4.5 mS/cm versus 47.8 mS/cm), and a higher concentration of sulfonated domains at the film's surface that reduced membrane-electrode interfacial resistance associated with the CCM. N212's greater conductivity (96.3 mS/cm) led to an MEA with much better PEMFC performance ([Fig. 8B](#)). At these operating

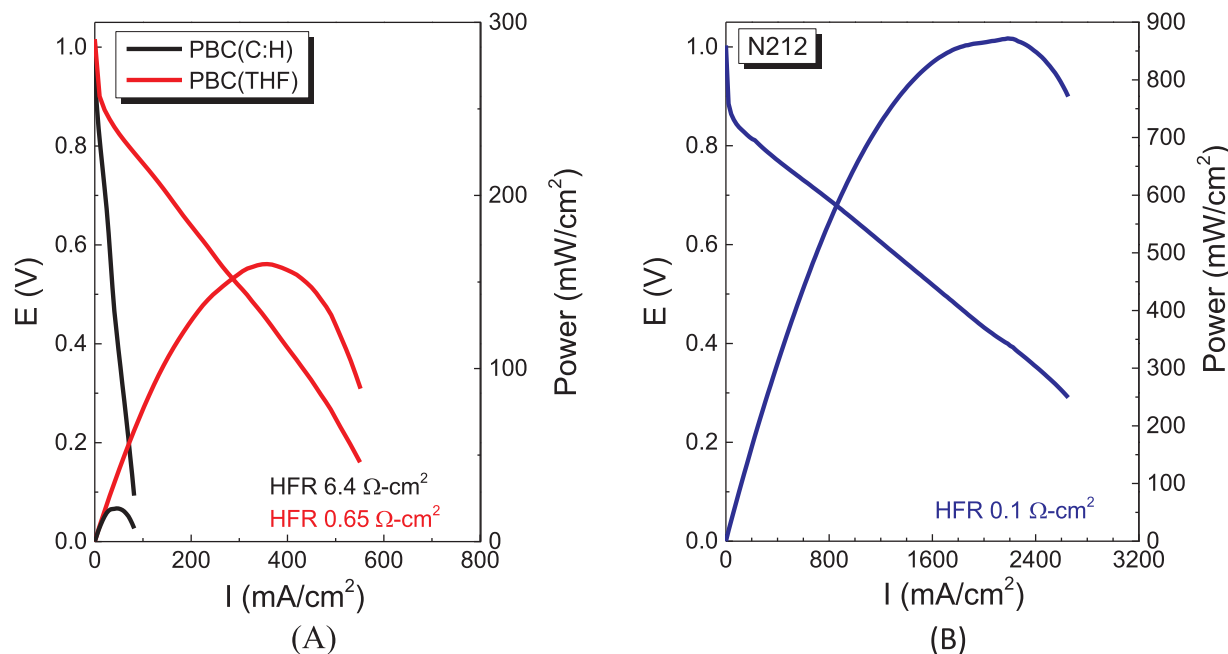


Fig. 8. PEMFC polarization curves using A) PBC(C:H) and PBC(THF); and B) N212 at 80 °C, 100% RH, 15 psig; and O₂ and H₂ flowing at 300 SCCM.

conditions and MEA catalyst loading, N212 had a peak power of 870 mW/cm² at 2100 mA/cm² and a membrane-electrode interfacial resistance of 0.1 Ω·cm². The interfacial resistance of N212 is 500% lower than PBC(THF) and 6300% lower than PBC(C:H); and its proton conductivity is 88% larger than PBC(THF) and 1900% greater than PBC(C:H). The non-random morphology of PBC(THF) led to a significant reduction between it and N212 PEMFC function. However, greater conductivity is needed in order for PBC to become a viable alternative, and creating an ionomer with distinct micro-phase separation is clearly required too.

3.6. PBC and N117 vanadium flow battery performance and chemical stability

VRB energy storage performance was evaluated using PBC(C:H), PBC(THF), and N117 to probe the role of morphology. Their individual charge-discharge profiles from 1.7 to 0.8 V at 10 mA/cm² and 25 °C with the electrolyte flowing at 20 mL/minute are shown in Fig. 9A. PBC(THF) and N117 possessed similar charge-discharge behavior relative to PBC(C:H). The larger difference between these ionomers may be due to the significantly lower conductivity of PBC(C:H). The battery cell's η_{CE} during charge and discharge cycles describes its capacity losses. Ionomer dependent properties are related to its IEC, thickness, processing method, composition, and morphology. Unwanted vanadium-ion crossover causes the cell to undergo self-discharge. Consequently, an ideal ionomer film will have highly selective proton transport, and its permeability to vanadium ions will be none. The η_{CE} of a PBC(C:H) film was 96.8%, which demonstrates that it has ion-selective permeability between a proton and a vanadium ion (Fig. 9B). PBC(THF)'s well-ordered morphology that improved proton conductivity due to greater ion-domain connectivity caused the cell's η_{CE} to decrease to 88.4%. This result implies that enhancing sulfonated-domain connectivity to increase proton conductivity does not ensure VRB improvements. These changes must be coupled with preserving small ion-channels that produces ion selectivity. N117 is known to have a random morphology that is bicontinuous with large sulfonated domains. Its in-plane conductivity is 90.4 mS/cm and much greater than both PBC films, but its η_{CE} is still poor at 83.7% [29].

A battery's ohmic resistance and polarization losses during cycling are described by its η_{VE} , which is largely affected by charge-carrier

mobility. As previously noted, PBC(C:H) low ion conductivity is attributed to smaller sulfonated domains that are poorly connected with each other. This morphology produced a η_{VE} of 62.7% that is lower than PBC(THF) with a η_{VE} of 71.2% (Fig. 9B). An increase in η_{VE} is due to enhanced sulfonated domain connectivity that improved charge-carrier mobility. The η_{VE} of N117 was 75.4% even though its in-plane ion conductivity was double PBC(THF), which only produced a 5.6% increase in η_{VE} . PBC(C:H), PBC(THF), and N117 values for η_{EE} were 60.6%, 63.0%, and 63.1% (Fig. 9B). This small variation between ionomer type and morphology versus η_{EE} is a surprising result. Several efforts suggest that diminished ion conductivity effects corresponding to VRB performance are due to its highly acidic operational environment [12,36,37]. This seems consistent with these η_{EE} results. However, ionomer morphology is still assumed to be a vital factor for the tunability of ion selectivity that should be important to redox flow batteries.

A VRB self-discharge is predominantly attributed to unwanted vanadium ion transport through a given membrane. These changes are primarily associated with ionomer type, ion-group concentration (IEC), ion-domain size, and spatial arrangement of ion-conductive groups. An OCV test versus time was used to measure the self-discharge behavior of PBC(C:H), PBC(THF), and N117. This experiment was done in order to examine the role of ionomer type and morphology that are summarized in Fig. 10. In all OCV experiments, a dramatic voltage rate of change occurs near 1.25 V. Due to the rapid voltage decay rate and inflection near this point; a voltage of 1.15 V was used as an endpoint for this test. The random PBC(C:H) morphology and low IEC produced the slowest VRB discharge rate. This battery required 12.2 days to decrease its OCV from 1.40 to 1.15 V. PBC(THF) improved morphology created to unwanted vanadium-ion transport leading to accelerated discharge from 1.35 to 1.15 V to occur in only 4.5 days. PBC(THF)'s enhanced morphology improved proton conductivity and fuel cell performance, but clearly lost ion-selectivity that is needed for a VRB. N117 was used as a comparison for PBC even though its proton conductivity is larger (90 mS/cm versus 4.5 and 47.8 mS/cm); and it is thicker than PBC (178.7 μm versus 90 μm). The time required to discharge from 1.36 to 1.15 V was 3 days. The accelerated OCV decline for PBC(THF) and N117 is believed to be due to larger ion-domain channels that are not ion-selective. SAXS and TEM results revealed that PBC(C:H)'s small and poorly connected domains led to a film with lower water swelling and

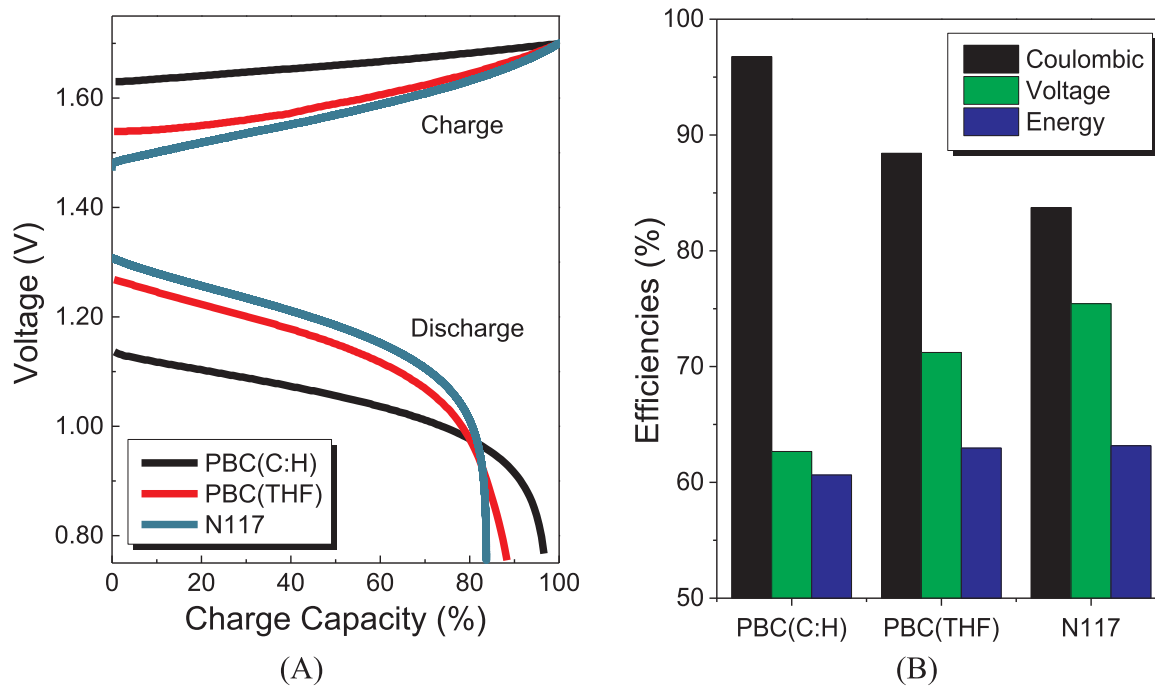


Fig. 9. PBC(C:H), PBC(THF), and N117 VRB function at 10 mA/cm² for A) VRB charge-discharge profiles; and B) coulombic, voltage, and total energy efficiency at 25 °C.

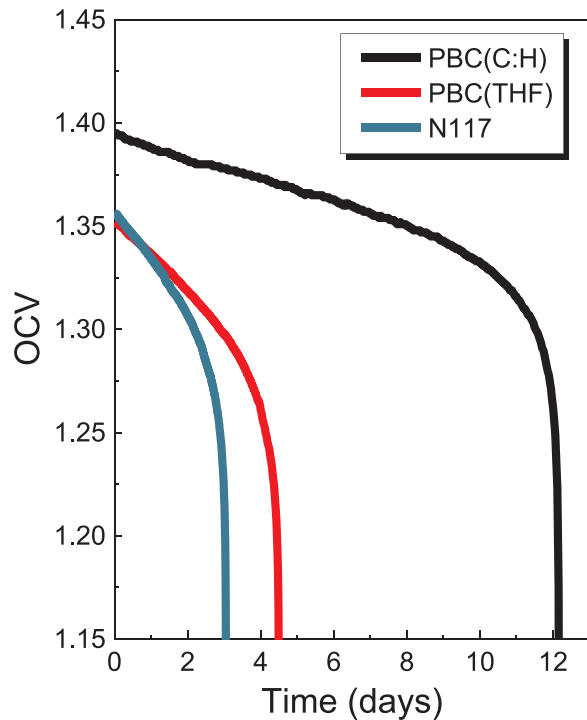


Fig. 10. VRB self-discharge test relating changes in OCV versus time for PBC(C:H), PBC(THF), and N117 using a cell containing 1.0 M V⁵⁺ in 2.5 M V H₂SO₄ at 25 °C.

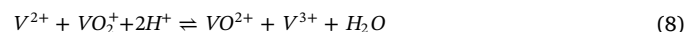
proton conductivity, but improved ion-selective transport. Overall, VRB selective-ion improvements must be related to attenuating ion-channel size as shown by this OCV test.

Assessing VRB performance is difficult because its function is dependent upon the cell's operating conditions and ionomer. *Ex-situ* VO²⁺ permeability studies are typically done to evaluate an ionomer's resistance to unwanted ion-transport. However, this test only provides an ideal representation of the dynamic nature of this system. In order to estimate VO²⁺ permeability through an ionomer within an operating

VRB cell, the steady-state OCV data was converted into vanadium and proton ion concentrations ($c_{VO_2^+}$, c_{H^+} , $c_{V^{2+}}$, $c_{VO^{2+}}$, and, $c_{V^{3+}}$) in mol/L. The ideal standard potential (E^\ominus) was evaluated at standard-state conditions is 1.237 V, which is determined at a concentration of 1 M, all specie activity coefficients (γ_i) equal to one, Faraday's constant (F), and E^\ominus at 25 °C [36]. These variables were used to model the reversible OCV (E_{rev}) described by the Nernst relationship (Eq. (7)).

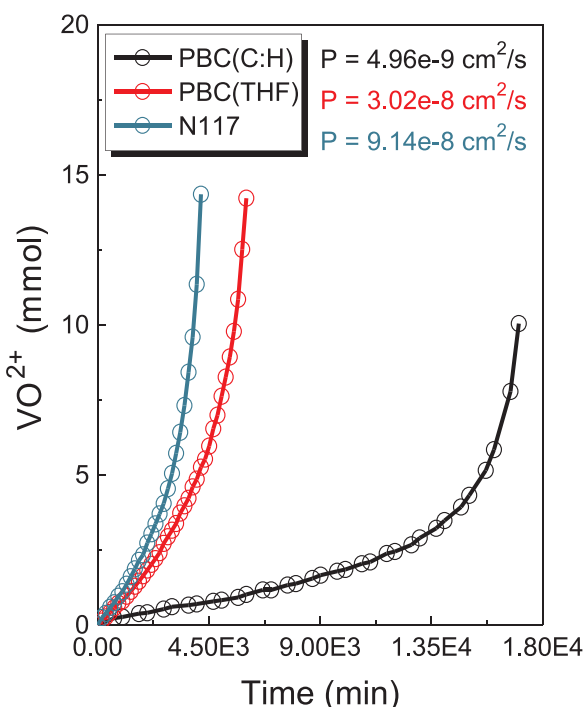
$$E_{rev} = E^\ominus + \frac{RT}{F} \ln \left[\left(\frac{c_{VO_2^+}(c_{H^+})^2}{c_{VO^{2+}}} \right) \left(\frac{c_{V^{2+}}}{c_{V^{3+}}} \right) \right] \quad (7)$$

The experimentally observed OCV is assumed to be at a pseudo steady-state vanadium ion concentrations. At these conditions, the overall equilibrium redox reaction during charge and discharge is given by Eq. (8).



The VRB cell's ohmic (E_{ohm}), concentration (E_{conc}), and activation (E_{pot}) overpotentials, which describe the total cell voltage (E_{cell}) were assumed to be negligible to nearly zero during an OCV test. This assumption is based upon the fact that the overpotentials represent the energy needed to force the redox reaction to proceed at a given current density (i). At OCV conditions, the VRB cell is operating with $i \approx 0$, which implies that E_{ohm} , E_{conc} , and E_{pot} overpotentials are small and $E_{cell} \approx E_{rev}$. Utilizing this assumption, the change in VO²⁺ concentration versus time was predicted using Eq. (7) and plotted in Fig. 11. VO²⁺ concentration increased rapidly for PBC(THF) and N117. The predicted VO²⁺ permeability was 3.02e-8 cm²/s for PBC(THF), and 9.14e-8 cm²/s for N117. This N117 result is 6.1% smaller than the ideal VO²⁺ permeability of 9.7e-8 cm²/s reported by Largier and Cornelius at the same concentration and temperature using a diffusion cell [37]. This result supports the $E_{cell} \approx E_{rev}$ assumption at OCV. The VO²⁺ permeability of PBC(C:H) was 4.96e-9 cm²/s, which is 5x smaller than PBC(THF), and 13x less than N117. These VO²⁺ permeability differences are quite significant, which reveals that morphology and conductivity must be properly attenuated to arrive at very ion-selective ionomers.

Several *ex-situ* strategies have been proposed to observe ionomer changes when exposed to reactive vanadium ion species within a VRB cell [38,39]. PBC(C:H), PBC(THF), and N117 chemical stability was



3 V [41]. While the displacements are differed from this work, it should be noted that the processing method and films were quite different. However, the result does reveal that PBC performs approximately 50% better than Nafion even with a random morphology. This result suggests that future IPMC research should consider both ionomer type and morphology when seeking to improve actuator performance.

4. Conclusions

The relationship between solution-casting an ionomer film and its properties are linked to morphology and the spatial arrangement of functional groups. Previous ionomer film studies attempting to control morphology, physical and transport properties, and degradation rate have focused upon processing method. Few research efforts have examined the importance of solution-casting related to ionomer film development. In this work, THF solution-cast PBC(THF) films exhibited a well-ordered lamella/hexagonally packed morphology as compared to a random structured created within a C:H solution cast PBC(C:H) film. This initial study demonstrated that an appropriate solvent (THF) altered proton transport properties at a constant IEC for PBC(THF). The ordered film's morphology led a 962% increase in proton conductivity. This research effort provides insight in regard to the significance of ionomer morphology related to improving the function of fuel cells, VRBs, and IPMC actuators. This research provides a framework for future studies related to improving ionomer conductivity and physical properties, which are linked to composition, ion-group concentration, and morphology.

Acknowledgments

This work was possible due to materials supplied by Dr. Carl Willis at Kraton Polymers LLC. Transmission electron microscopy (TEM) was performed by Dr. Han Chen in the Morrison Microscopy Core Research Facility at UNL Biotechnology Center. Funding by a grant from the Nebraska Center for Energy Sciences Research Cycle 11 at the University of Nebraska-Lincoln enabled major portions of this work.

References

- [1] T. Sata, Ion Exchange Membranes: Preparation, Characterization, Modification and Application, Royal Society of chemistry, 2004.
- [2] A. Eisenberg, H.L. Yeager, Perfluorinated Ionomer Membranes, American Chemical Society, 1982.
- [3] A. Eisenberg, J.-S. Kim, Introduction to Ionomers, Wiley, 1998.
- [4] K. Kreuer, On the development of proton conducting polymer membranes for hydrogen and methanol fuel cells, *J. Membr. Sci.* 185 (2001) 29–39.
- [5] K. Sopian, W.R. Wan Daud, Challenges and future developments in proton exchange membrane fuel cells, *Renew. Energy* 31 (2006) 719–727.
- [6] T.A. Zawodzinski, T.E. Springer, J. Davey, R. Jestel, C. Lopez, J. Valerio, S. Gottesfeld, A comparative study of water uptake by and transport through ionomeric fuel cell membranes, *J. Electrochem. Soc.* 140 (1993) 1981–1985.
- [7] M. Shahinpoor, K.J. Kim, Ionic polymer-metal composites: I. Fundamentals, *Smart Mater. Struct.* 10 (2001) 819–833.
- [8] M. Shahinpoor, Y. Bar-Cohen, J. Simpson, J. Smith, Ionic polymer-metal composites (IPMCs) as biomimetic sensors, actuators and artificial muscles-a review, *Smart Mater. Struct.* 7 (1998) R15.
- [9] S. Nemat-Nasser, Micromechanics of actuation of ionic polymer-metal composites, *J. Appl. Phys.* 92 (2002) 2899–2915.
- [10] K. Asaka, K. Oguro, Y. Nishimura, M. Mizuhata, H. Takenaka, Bending of poly-electrolyte membrane-platinum composites by electric stimuli I. Response characteristics to various waveforms, *Polym. J.* 27 (1995) 436–440.
- [11] W. Zheng, C. Cornelius, Solvent tunable multi-block ionomer morphology and its relationship to modulus, water swelling, directionally dependent ion transport, and actuator performance, *Polymer* 103 (2016) 104–111.
- [12] Z. Mai, H. Zhang, X. Li, C. Bi, H. Dai, Sulfonated poly (tetramethyldiphenyl ether ether ketone) membranes for vanadium redox flow battery application, *J. Power Sources* 196 (2011) 482–487.
- [13] X. Li, H. Zhang, Z. Mai, H. Zhang, I. Vankelecom, Ion exchange membranes for vanadium redox flow battery (VRB) applications, *Energy Environ. Sci.* 4 (2011) 1147–1160.
- [14] D. Nguyen, C.E. Williams, A. Eisenberg, Block ionomer micelles in solution. 1. characterization of ionic cores by small-angle X-ray scattering, *Macromolecules* 27 (1994) 5090–5093.
- [15] C. Heitner-Wirguin, Recent advances in perfluorinated ionomer membranes: structure, properties and applications, *J. Membr. Sci.* 120 (1996) 1–33.
- [16] R. Silva, M. De Francesco, A. Pozio, Solution-cast Nafion® ionomer membranes: preparation and characterization, *Electrochim. Acta* 49 (2004) 3211–3219.
- [17] L.H. Sperling, Introduction to Physical Polymer Science, John Wiley & Sons, 2005.
- [18] C. Zhao, H. Lin, K. Shao, X. Li, H. Ni, Z. Wang, H. Na, Block sulfonated poly(ether ether ketone)s (SPEEK) ionomers with high ion-exchange capacities for proton exchange membranes, *J. Power Sources* 162 (2006) 1003–1009.
- [19] H.S. Lee, A.S. Badami, A. Roy, J.E. McGrath, Segmented sulfonated poly(arylene ether sulfone)-b-polyimide copolymers for proton exchange membrane fuel cells. I. copolymer synthesis and fundamental properties, *J. Polym. Sci. Part A: Polym. Chem.* 45 (2007) 4879–4890.
- [20] Y. Fan, M. Zhang, R.B. Moore, H.-S. Lee, J.E. McGrath, C.J. Cornelius, Viscoelastic and gas transport properties of a series of multiblock copolymer ionomers, *Polymer* 52 (2011) 3963–3969.
- [21] C.-H. Ma, T.L. Yu, H.-L. Lin, Y.-T. Huang, Y.-L. Chen, U.S. Jeng, Y.-H. Lai, Y.-S. Sun, Morphology and properties of Nafion membranes prepared by solution casting, *Polymer* 50 (2009) 1764–1777.
- [22] Z. Siroma, N. Fujiwara, T. Irori, S. Yamazaki, K. Yasuda, Y. Miyazaki, Dissolution of Nafion® membrane and recast Nafion® film in mixtures of methanol and water, *J. Power Sources* 126 (2004) 41–45.
- [23] G.P. Robertson, S.D. Mikhailenko, K. Wang, P. Xing, M.D. Guiver, S. Kaliaguine, Casting solvent interactions with sulfonated poly(ether ether ketone) during proton exchange membrane fabrication, *J. Membr. Sci.* 219 (2003) 113–121.
- [24] P. Bébin, H. Galiano, Processing of PEMFC membranes by extrusion: part 1. Sulfonated polysulfone in acid form, *Adv. Polym. Technol.* 25 (2006) 121–126.
- [25] P. Bébin, H. Galiano, Processing of sulfonated polysulfone for PEMFC membrane applications: part 2. Polymer in salt form, *Adv. Polym. Technol.* 25 (2006) 127–133.
- [26] D. Wang, C.J. Cornelius, Modeling ionomer swelling dynamics of a sulfonated Polyphenylene, Pentablock copolymers, and Nafion, *J. Polym. Sci. Part B: Polym. Phys.* 55 (5) (2017) 435–443.
- [27] J.-H. Choi, A. Kota, K.I. Winey, Micellar morphology in sulfonated pentablock copolymer solutions, *Ind. Eng. Chem. Res.* 49 (2010) 12093–12097.
- [28] G. Gebel, Structural evolution of water swollen perfluorosulfonated ionomers from dry membrane to solution, *Polymer* 41 (2000) 5829–5838.
- [29] K.A. Mauritz, R.B. Moore, State of understanding of Nafion, *Chem. Rev.* 104 (2004) 4535–4586.
- [30] D.W. Van Krevelen, K. Te Nijenhuis, Properties of Polymers: Their Correlation With Chemical Structure; Their Numerical Estimation and Prediction From Additive Group Contributions, Elsevier, 2009.
- [31] X. Lu, R.A. Weiss, Development of Miscible Blends Of Bisphenol A Polycarbonate And Lightly Sulfonated Polystyrene Ionomers From Intrapolymer Repulsive Interactions, *Macromolecules* 29 (1996) 1216–1221.
- [32] L.M. Robeson, Polymer Blends, Hanser, Munich, 2007, pp. 24–149.
- [33] M.J. Forrest, Rubber Analysis: Polymers, Compounds and Products, iSmithers Rapra Publishing, 2001.
- [34] P.J. Flory, Thermodynamics of high polymer solutions, *J. Chem. Phys.* 9 (1941) (660–660).
- [35] D. Wang, C.J. Cornelius, Ionomer thermodynamic interrelationships associated with wettability, surface energy, swelling, and water transport, *Eur. Polym. J.* 85 (2016) 126–138.
- [36] J.-Y. Chen, C.-L. Hsieh, N.-Y. Hsu, Y.-S. Chou, Y.-S. Chen, Determining the limiting current density of vanadium redox flow batteries, *Energies* 7 (2014) 5863–5873.
- [37] T.D. Largier, C.J. Cornelius, Random quaternary ammonium diels-alder poly(phenylene) copolymers for improved vanadium redox flow batteries, *J. Power Sources* 352 (2017) 149–155.
- [38] S. Kim, T.B. Tighe, B. Schwenzer, J. Yan, J. Zhang, J. Liu, Z. Yang, M.A. Hickner, Chemical and mechanical degradation of sulfonated poly (sulfone) membranes in vanadium redox flow batteries, *J. Appl. Electrochem.* 41 (2011) 1201–1213.
- [39] D. Chen, M.A. Hickner, V5+ degradation of sulfonated Radel membranes for vanadium redox flow batteries, *Phys. Chem. Chem. Phys.* 15 (2013) 11299–11305.
- [40] A. Khan, M. Luqman, A. Dutta, Kraton based ionic polymer metal composite (IPMC) actuator, *Sens. Actuators A: Phys.* 216 (2014) 295–300.
- [41] K.A. Inamuddin, R.K. Jain, M. Naushad, Development of sulfonated poly(vinyl alcohol)/polypyrrole based ionic polymer metal composite (IPMC) actuator and its characterization, *Smart Mater. Struct.* 24 (9) (2015) 095003.
- [42] M.L. Huggins, Solutions of long chain compounds, *J. Chem. Phys.* 9 (9) (1941) 440.